Title

In situ TEM study of the thermal stability of nanotwinned Ni-Mo-W alloys

Journal

Materials Research Letters, 11(10)

ISSN

2166-3831

Authors

He, Mo-Rigen

Zhang, Ruopeng

Dhall, Rohan

et al.

Publication Date

2023-10-03

DOI

10.1080/21663831.2023.2255321

Materials Research Letters

ISSN: (Print) (Online) Journal homepage: https://www.tandfonline.com/loi/tmrl20

In situ TEM study of the thermal stability of nanotwinned Ni-Mo-W alloys

Mo-Rigen He, Ruopeng Zhang, Rohan Dhall, Andrew M. Minor & Kevin J. Hemker

To cite this article: Mo-Rigen He, Ruopeng Zhang, Rohan Dhall, Andrew M. Minor & Kevin J. Hemker (2023) In situ TEM study of the thermal stability of nanotwinned Ni-Mo-W alloys, Materials Research Letters, 11:10, 879-887, DOI: 10.1080/21663831.2023.2255321

To link to this article: https://doi.org/10.1080/21663831.2023.2255321

Published online: 11 Sep 2023.

MATER. RES. LETT.
2023, VOL. 11, NO. 10, 879–887
https://doi.org/10.1080/21663831.2023.2255321

MATERIALS RESEARCH LETTERS
Taylor & Francis
Taylor & Francis Group

ORIGINAL REPORTS

In situ TEM study of the thermal stability of nanotwinned Ni-Mo-W alloys

Mo-Rigen He[a], Ruopeng Zhang [b,c], Rohan Dhall[b,c], Andrew M. Minor[b,c] and Kevin J. Hemker[a]

[a]Department of Mechanical Engineering, Johns Hopkins University, Baltimore, MD, USA; [b]Department of Materials Science & Engineering, University of California, Berkeley, CA, USA; [c]National Center for Electron Microscopy (NCEM), Lawrence Berkeley National Laboratory, Berkeley, CA, USA

ABSTRACT

Microstructural evolution in nanotwinned Ni-Mo-W alloys under *in situ* heating experiments is investigated in a transmission electron microscope. Migration of twin boundaries and grain boundaries as well as formation of carbide precipitates are observed at various temperatures and characterized at atomic resolution. These transformations are found to occur at temperatures that are ~200°C lower in Mo-rich ($Ni_{85}Mo_{13}W_2$) specimens than in W-rich ($Ni_{86}Mo_3W_{11}$) specimens, which highlights the different efficacy of Mo and W solutes in stabilizing the nanotwinned structure. Inspection of various mechanisms points to the importance of elastic modulus mismatch as a pathway for enhancing nanotwin stability by alloying.

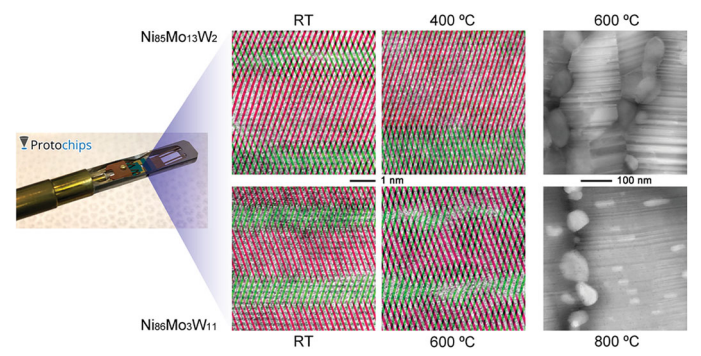

IMPACT STATEMENT

We present the first *in situ* and atomic-resolution study of the thermal stability of nanotwinned alloys. Comparison of Mo-rich and W-rich Ni-Mo-W alloys uncovers the nontrivial role of solute species.

ARTICLE HISTORY
Received 28 June 2023

KEYWORDS
Nickel alloys; nanotwin; TEM; thermal stability; solute strengthening

Introduction

Nanotwinned materials have gained rising attention over the last few decades [1–3] due to their desirable combination of high strength, good ductility, and superior electrical conductivity, as typically shown in nanotwinned Cu [4–6]. However, notable detwinning and grain growth under thermal or mechanical loads [7–9] precludes the employment of nanotwinned Cu (and similar monolithic metals) in extreme environments, such as high temperature microelectromechanical systems (MEMS), which require structural materials with good dimensional and microstructural stability [10]. In some cases nanotwinned alloys were found to be more stable [11]; in particular, densely packed nanotwins were present in some alloys of metals (e.g. Ni, Al) [12,13] with otherwise much higher stacking fault energy (SFE) than Cu.

Nanotwinned Ni-Mo-W alloys have recently been shown to possess a unique suite of properties, including ultrahigh mechanical strength (> 3 GPa), tailorable coefficient of thermal expansion (CTE), and improved microstructural stability [14–16], making them promising candidates for high temperature applications. For instance, heat treatments of a $Ni_{84}Mo_{14}W_2$ film (all compositions hereinafter are atomic fractions) exhibited good stability of the as-deposited columnar grains with ultrafine nanotwins when annealed at 600°C for 1 h, whereas detwinning, recrystallization, and precipitate formation were associated with 800°C and 1000°C annealing [15].

CONTACT Mo-Rigen He mrigen1@jhu.edu; Kevin J. Hemker hemker@jhu.edu Department of Mechanical Engineering, Johns Hopkins University, Baltimore, MD 21218, USA

These results accord well with the prediction of first-principle calculations [17], i.e. Mo and W solutes effectively decrease the SFE in pure Ni and therefore promote the formation and stability of nanotwins [12].

The relation between microstructure and physical properties in these alloys, however, remains less understood. For example, CTE values in a series of $Ni_{85}Mo_xW_{15-x}$ films ($x = 0 \sim 15$) exhibited invariance with temperature (in the range of 20 ~ 600°C) for the Mo-rich films, in contrast to positive temperature dependence for the W-rich films [16], the latter being comparable to that in pure Ni and many of its binary alloys [18–20]. These results indicate that Mo and W solutes behave differently in the nanotwinned Ni-Mo-W alloys, but the microscopic mechanism that underpins this difference has yet to be clarified. Relatedly, the likely different efficacy of Mo and W that affects the microstructural stability of nanotwinned alloys also need to be assessed, which is a prerequisite for optimizing and utilizing their unique thermomechanical behaviors. In the present study, we utilize direct atomic-scale observations during *in situ* heating to investigate the relative thermal stability of two Ni-Mo-W alloys. Possible controlling mechanisms are investigated to discern the role of different solute species.

Materials and methods

Nanotwinned Ni-Mo-W alloys were investigated with *in situ* heating experiments inside the TEAM I (NCEM), a double-corrected microscope operated in scanning transmission electron microscope (STEM) mode at 300 kV. Temperature-controlled annealing was implemented using the Fusion Select holder (Protochips Inc.), wherein microscopic specimens were attached to a MEMS-based heating element [21], as shown in Figure 1(a and b). This approach minimizes specimen drift at elevated temperatures and provides a precise measurement of the local temperature. Two batches of films with comparative compositions of $Ni_{85}Mo_{13}W_2$ and $Ni_{86}Mo_3W_{11}$ (hereinafter denoted as Mo-rich and W-rich specimens) were synthesized with magnetron sputter deposition [14] and used for specimen fabrication inside a Helios G4 UC DualBeam system (ThermoFisher Scientific). As demonstrated in Figure 1(c and d), thin foils were extracted from the films using 30 kV Ga^+ focused ion beam (FIB) and polished to 100 nm or less in thickness using 2 kV Ga^+. Each foil was then attached to a MEMS chip using FIB-assisted deposition of Pt/C, with the area of interest supported over a through hole (8 μm in diameter) in the SiN membrane heater.

For each specimen, a columnar grain was selected and oriented along the common $[1\bar{1}0]$ zone axis of the nanotwins, with the (111) twin boundaries (TBs) viewed edge-on. Double-axis tilting was facilitated by the Fusion Select holder, allowing for precise alignment and atomic-resolution imaging of the ultrafine (typically < 5 nm) nanotwins. The specimens were heated stepwise from room temperature (RT) with an increment of 100°C over 1 min; the studied grain was allowed to stabilize for ~2 min, and then characterized in STEM high-angle annular dark field (HAADF) mode while the temperature was held constant for a duration up to 30 min. Microstructural evolution in the Mo-rich and W-rich specimens are delineated and compared in detail in the remainder of this letter, but an overview of the entire process is helpful here. The nanotwinned structure remained stable at low temperatures near RT; migration of TBs and grain boundaries (GBs) then initiated and proceeded slowly at intermediate temperatures (see Figures 2 and 3);

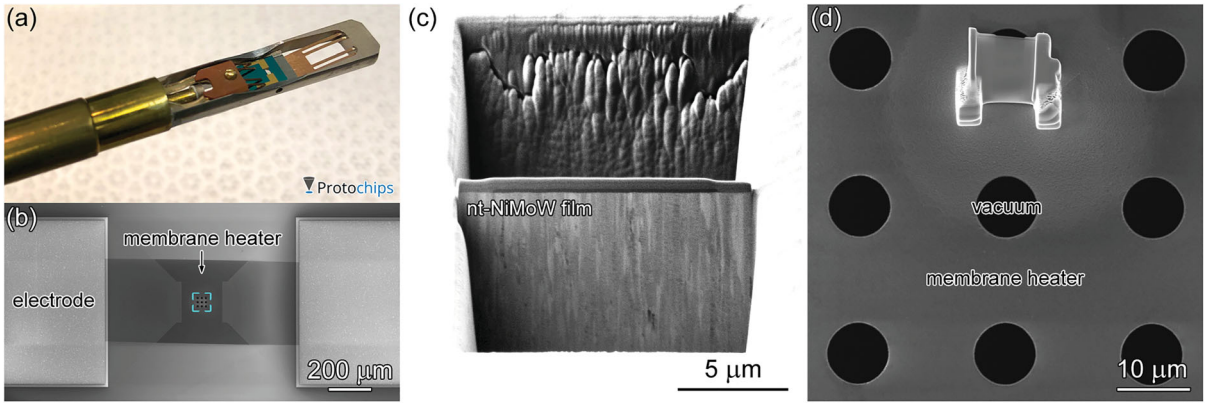

Figure 1. Experimental setup for *in situ* heating. **(a)** Photograph of Fusion Select TEM holder (Protochips Inc.); **(b)** SEM image of the functional area of a MEMS heating chip (Protochips Inc.); **(c)** Representative cross-sectional view of a nanotwinned Ni-Mo-W film used for this study, the columnar grains are visible with ion channeling contrast; **(d)** SEM image of a thin foil that was lifted out and transferred onto the MEMS chip (box area in b).

nanosized precipitates were generated and the specimens rapidly degraded at higher temperatures (see Figures 4 and 5). It was noted that, for each stage of microstructural evolution, the onset temperature in the Mo-rich specimens was ~200°C lower than in the W-rich specimens.

Results and discussions

Thermal migration of the TBs in the Mo-rich specimens is described first and demonstrated in Figure 2. An [1$\bar{1}$0] oriented grain is shown at RT in Figure 2(a1). The two twinning variants, arbitrarily denoted as matrix (pink) and twin (green), are distinguishable in the atomic-resolution STEM HAADF image and are highlighted by applying Fourier Transform filtering (see inset). Closer examination reveals that the (111) coherent TBs in the as-made Ni-Mo-W films were not atomically flat but contained steps (partial dislocations or disconnections), as marked with '∗' in Figure 2(a1) and typically identified in a magnified view in Figure 2(b). Such defective sites have also been observed in nanotwinned Cu [22–24] and associated with the migration of TBs under thermal or mechanical loads. In this Mo-rich specimen, TB migration was observed when the foil was heated to 400°C, see Figure 2(a2). The evolution of individual nanotwins are further evidenced in Figure 2(c) by comparing the intensity profiles of the Fourier filtered images as measured across the TBs (e.g. along the open arrows in Figure 2,

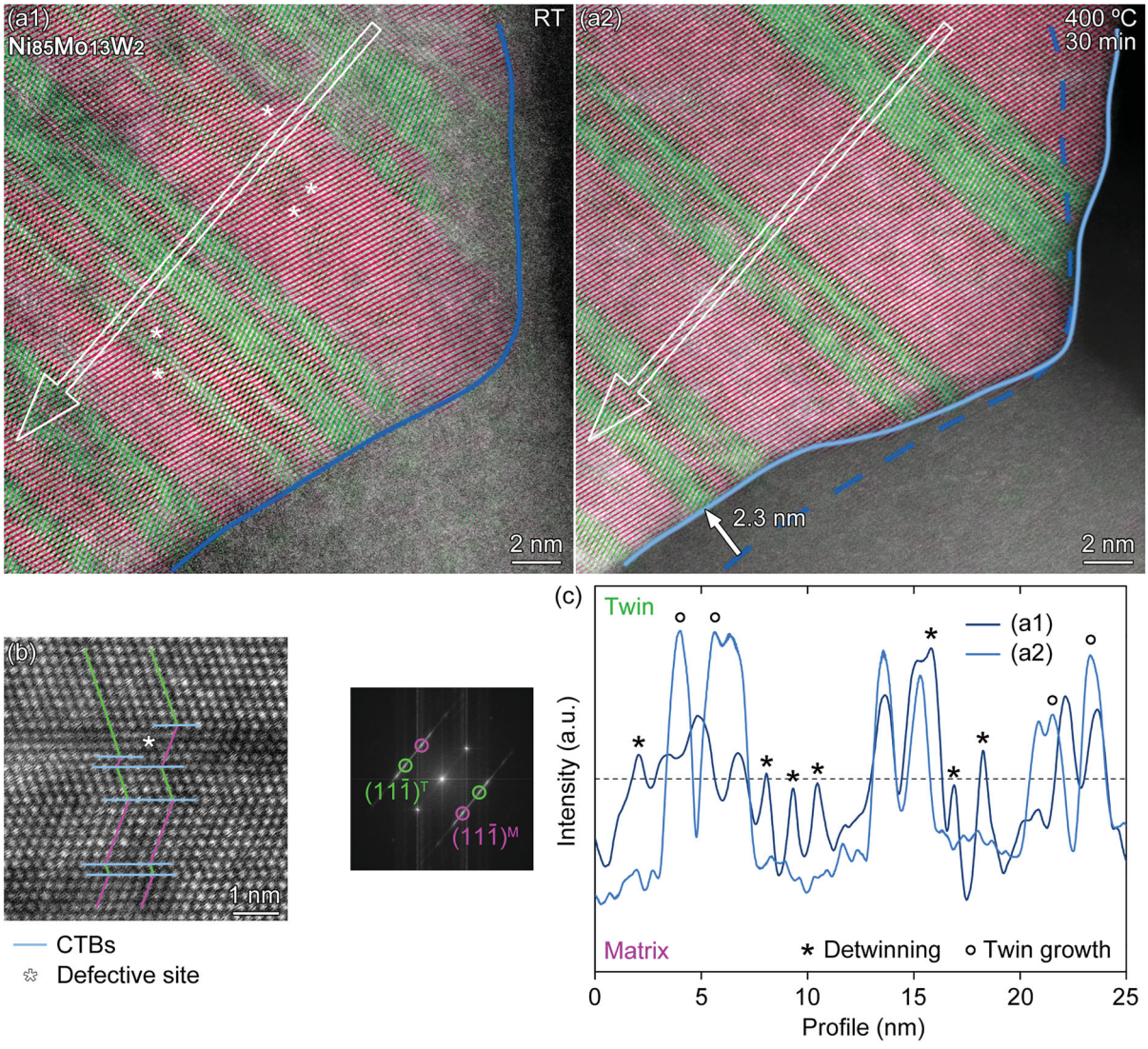

Figure 2. Migration of TBs and GBs in a Mo-rich specimen during *in situ* heating. **(a1)** STEM HAADF image of a columnar nanotwinned grain at RT: matrix (pink) and twin (green) variants are highlighted by filtering using corresponding 111 spots in the Fourier Transform pattern (inset), '∗' symbols indicate atomic steps on TBs, solid line (blue) is the initial position of GB; **(a2)** Fourier filtered image of the same area in (a1) after 30 min heating at 400°C: dash line (blue) is duplicated from (a1), solid line (light blue) is the position of the migrated GB; **(b)** Magnified view of a disconnection on TB (image is rotated with relative to (a1) and (a2)); **(c)** Intensity profiles as measured along the open arrows in (a1) and (a2). The difference between profiles (a1) and (a2) are marked as detwinning (∗) or twin growth (o) events.

a1 and a2, using a line width of 2 nm). Herein, the discernible valleys and peaks are identified as the matrix and twin variants, respectively. Therefore, the vanishing or narrowing peaks in profile (a1) indicate detwinning events, whereas the widening peaks in profile (a2) indicate growing twins. It is noteworthy that the atomic steps observed in Figure 2(a1) were all annihilated and no longer visible after *in situ* annealed at 400°C for 30 min.

The GBs between columnar grains were also observed to migrate when this foil was heated to 400°C. For the grain in Figure 2, the before and after position (projective trace) of the GB are marked with dashed and solid lines in Figure 2(a2). This GB was displaced by several nanometers in 30 min. Since this GB was a non-special type (i.e. low-angle or random high-angle), its thermal-activated migration to reduce the total interfacial energy is reasonable.

In sharp contrast to the Mo-rich specimens, the nanotwins in the W-rich specimens were found to be much more stable, indicating that the TBs are less mobile even at elevated temperatures. For instance, Figure 3 (a1 and a2) shows the same grain viewed in STEM HAADF mode at RT and after being *in situ* annealed at 600°C for 30 min. Following the same approach as above, both images were processed with Fourier Transform (see inset) filtering to highlight the matrix (pink) and twin (green) variants. The intensity profiles shown in Figure 3(c) were measured across the TBs (e.g. along the open arrows in Figure 3, a1 and a2, using a line width of 2 nm), and the positions of primary valleys and peaks were found

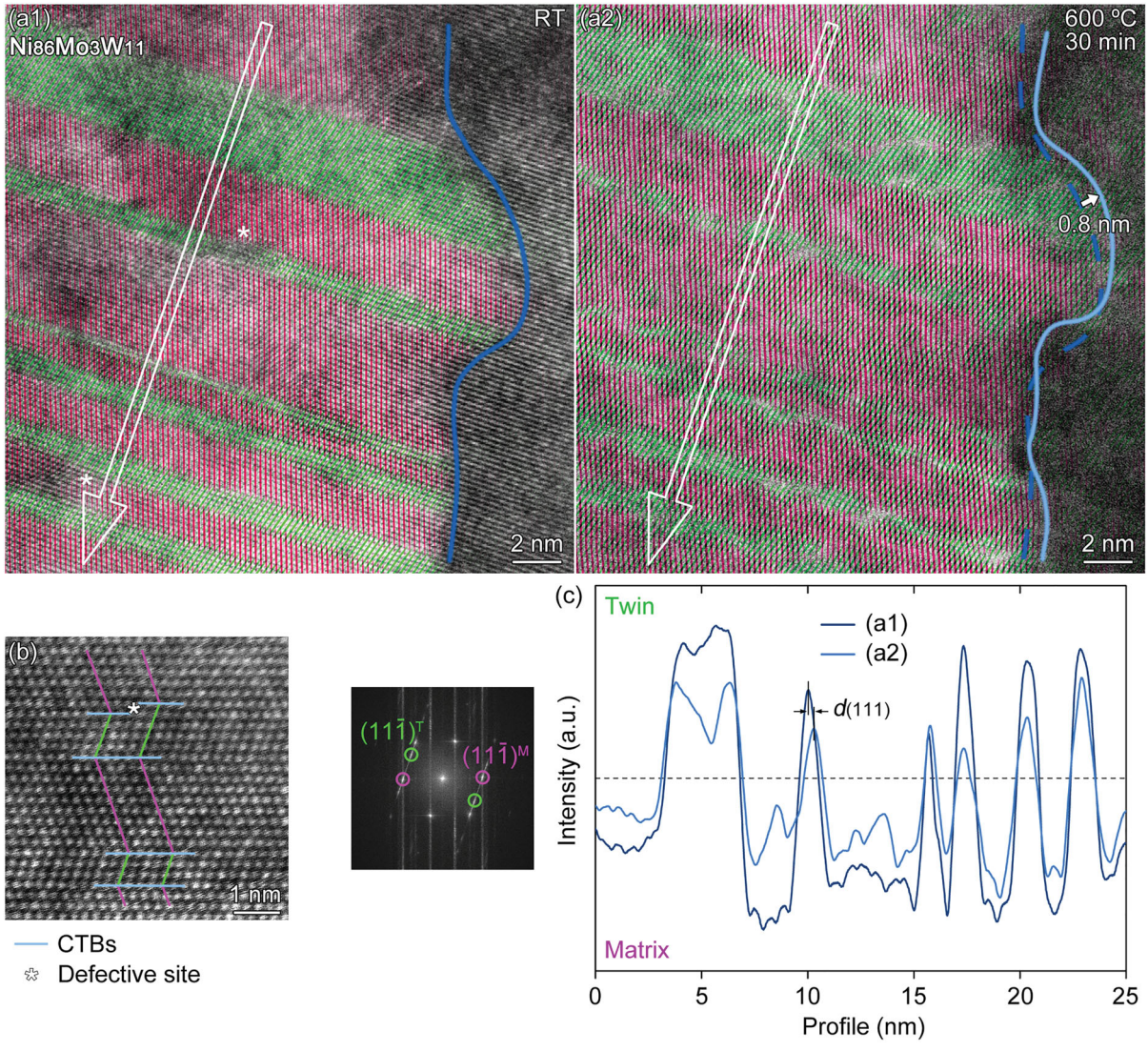

Figure 3. Migration of TBs and GBs in a W-rich specimen during *in situ* heating. **(a1)** Fourier filtered (inset) STEM HAADF image of a columnar nanotwinned grain at RT; **(a2)** the same area in (a1) after 30 min heating at 600°C; defective sites on TBs and positions of GB are marked likewise as in Figure 2; **(b)** Magnified view of an atomic step on TB (image is rotated with relative to (a1) and (a2)); **(c)** Intensity profiles as measured along the open arrows in (a1) and (a2).

to be almost unchanged, i.e. no greater than one layer thickness of (111) plane, at RT and 600°C. A few steps or disconnections were also observed on the TBs at RT, as marked with '∗' in Figure 3(a1) and shown in a magnified view in Figure 3(b). The lower resolution at 600°C made it unclear whether the atomic steps have migrated in Figure 3(a2); nevertheless, the measurements in Figure 3(c) convincingly proved that the nanotwinned structure was stable down to the atomic scale.

GBs appeared to migrate a little when this W-rich specimen was heated to 600°C, but they were much less mobile than in the Mo-rich specimen. For the grain in Figure 3 (a1 and a2), the GB (projected trace) was displaced less than a nanometer in 30 min. This observation is consistent with previous reports that alloying with W effectively improved the thermodynamic stability of nanocrystalline Ni by decreasing GB energies [25,26]. Likewise, the driving force of migration for the columnar GBs in our nanotwinned alloys may have been suppressed by W solutes.

In situ heating of both specimens at even higher temperatures ended with rapid formation of precipitates, which were later identified with STEM imaging and X-ray energy dispersive spectroscopy (XEDS) mapping after the specimens were cooled down to RT. In the Mo-rich specimens, all precipitates were found to nucleate on the columnar GBs and grow to ∼100 nm in diameter within 5 min at 600°C, see for example Figure 4(a). With XEDS maps (Figure 4(b)) and atom-resolved STEM HAADF image (Figure 4(c)), the precipitates were identified as Mo-rich M_2C carbide (space group: $P6_3/mmc$). Their averaged composition was $(Ni_{0.01}Mo_{0.90}W_{0.09})C_{0.44}$. No specific orientation relation was noticed between the precipitates and the nanotwinned grains.

In the W-rich specimens, significant precipitation only occurred when heated to 800°C; the precipitates nucleated both at the columnar GBs and inside the nanotwinned grains, and Figure 5 shows that both forms were identified as W-rich M_2C carbide (space group: $P6_3/mmc$ or $P\bar{3}m1$) with an averaged composition of $(Ni_{0.05}Mo_{0.45}W_{0.50})C_{0.56}$. Not explicitly shown here but similar to those in the Mo-rich specimens, no orientation relation was specified for the coarser precipitates (∼100 nm in diameter) on GBs. By contrast, the finer precipitates (∼10 nm in thickness) inside nanotwinned grains occasionally have their $(10\bar{1}0)$ planes aligned with the (111) twin planes, as revealed in Figure 5(c).

Taken as a whole, these *in situ* heating experiments of nanotwinned Ni-Mo-W alloys showed clear evidence of

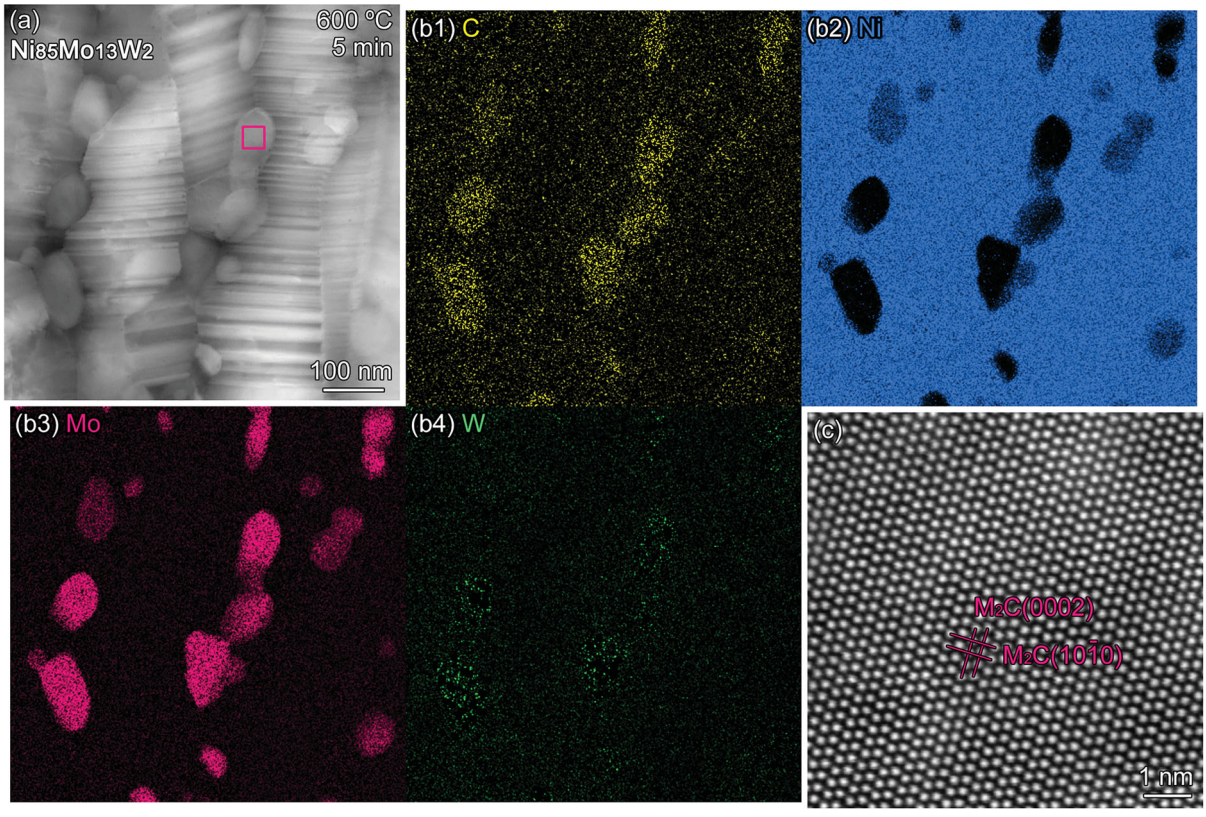

Figure 4. Precipitates formed in a Mo-rich specimen at 600°C (in 5 min). **(a)** STEM ADF image of the post-heated nanotwinned film; **(b1-b4)** XEDS maps of C, Ni, Mo and W; **(c)** representative atom-resolved HAADF image of a precipitate on the GB (box area in a).

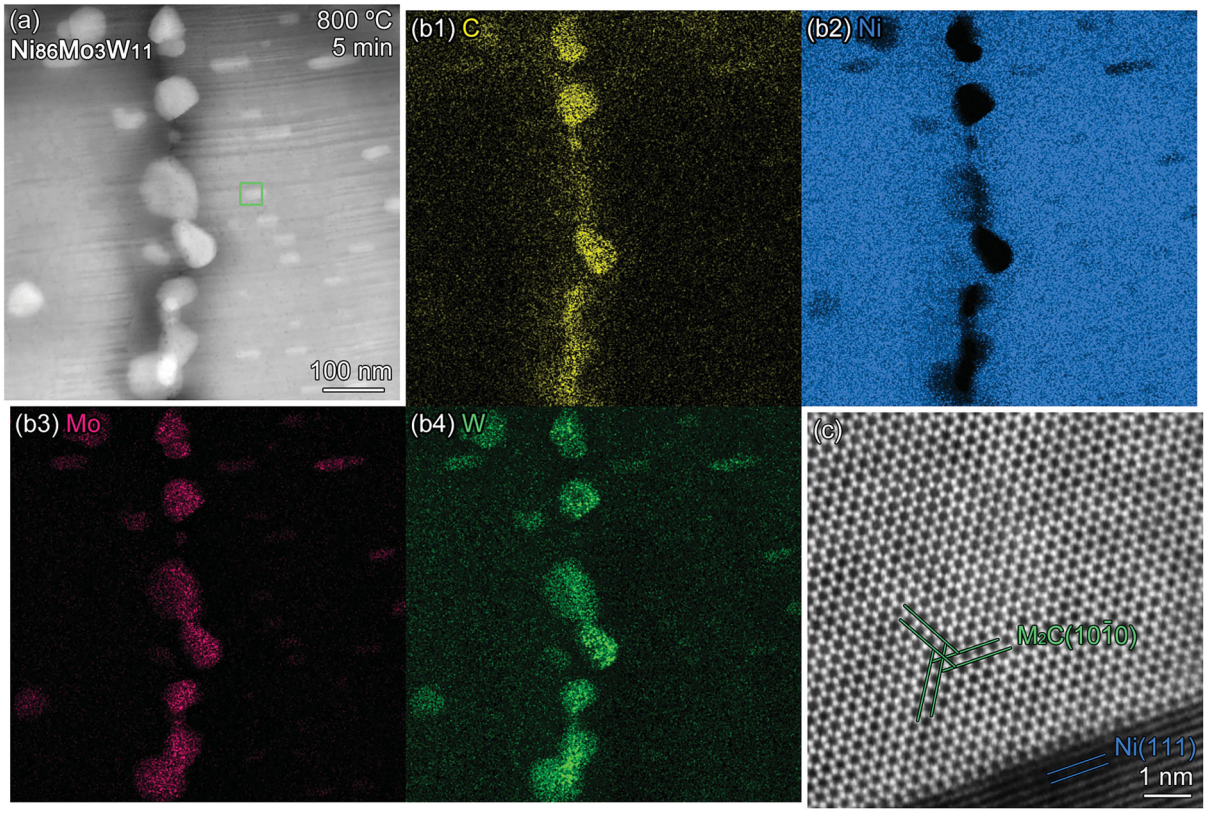

Figure 5. Precipitates formed in a W-rich specimen at 800°C (in 5 min). **(a)** STEM ADF image of the post-heated nanotwinned film; **(b1-b4)** XEDS maps of C, Ni, Mo and W; **(c)** representative atom-resolved HAADF image of a fine precipitate inside the nanotwinned grain (box area in a).

microstructural evolution and that changes in the Mo-rich specimens occurred at ~200°C lower temperatures than in the W-rich specimens. Whereas these temperatures may not be directly compared with those measured in other nanotwinned materials (typically with *ex situ* heating), the relative difference between Mo-rich and W-rich specimens is still meaningful. However, we first note that the role of alloy composition on thermal stability cannot be explained by the simple rule-of-mixtures of the homologous temperatures. Based on binary phase diagrams of Ni-Mo and Ni-W [27], the melting temperatures of $Ni_{85}Mo_{15}$ and $Ni_{85}W_{15}$ are estimated as 1430°C and 1500°C, respectively. It is therefore presumable that the melting temperatures of the two alloys ($Ni_{85}Mo_{13}W_2$ and $Ni_{86}Mo_3W_{11}$) studied here differ by no more than 50°C, so this factor alone cannot be used to describe the better stability of W-rich specimens than Mo-rich.

Difference in SFE would also affect the thermodynamic stability of nanotwins. First-principles calculations suggested that Mo and W solutes (which were intentionally placed on TBs) are very closely effective at decreasing the SFE in Ni [17]. The SFE of $Ni_{71}Mo$ and $Ni_{71}W$ was calculated to be 103.0 and 105.4 mJ/m^2, respectively (pure Ni was 132.1 mJ/m^2). The temperature dependence of SFE in Ni-Mo and Ni-W was also similar. However, the segregation behavior of Mo and W solutes in Ni could be different and deserves further attention. A semi-empirical model for binary alloys [28] was used to calculate the enthalpy of mixing to be −7 kJ/mol for Ni-Mo and −3 kJ/mol for Ni-W, suggesting that local ordering is comparatively more favored for Ni-Mo alloys and solute segregation to GBs is favored for Ni-W alloys. The latter was considered to account for the improved thermal stability of nanocrystalline Ni-W alloys [25]. In the nanotwinned Ni-Mo-W alloys studied here, however, STEM-XEDS analysis of both types of as-deposited films (see Appendix A) have yet to find convincing evidence of solute segregation at TBs. Moreover, no secondary phase at TBs or GBs was discernable during *in situ* heating, until the formation of carbides at much higher temperatures. As such, the contrasting thermal stability does not appear to be caused by differential segregation or precipitation, and are likely reflective of the different ways that Mo and W solutes interact with and inhibit TB/GB migration.

The kinetics of interfaces (and linear defects as well) can be influenced by solute drag, which is known to be governed by solute diffusion [29]. However, direct comparison (e.g. Figures 2 and 3) indicates that

W is more effective than Mo in stabilizing TBs/GBs even at higher temperatures. Extrapolating from the reported results in Ni-Mo and Ni-W systems [30–32], tracer diffusion coefficients of Mo/W in Ni were calculated to be $(0.4 \sim 12.1) \times 10^{-26}$ m^2/s at 400°C and $(0.4 \sim 6.9) \times 10^{-21}$ m^2/s at 600°C. Even though Mo diffuses slightly (1 order of magnitude) faster than W at identical temperatures, the ability of either species to drag an interface would be much (5 orders of magnitude) less at lower temperatures. The better stability of W-rich specimens than Mo-rich therefore cannot be attributed to solute diffusion and requires closer inspection.

The interaction between solutes and the atomic-scale defects at TBs is another considerable factor that controls their kinetics. This resembles the classic Fleischer model of solid solution strengthening [33] or the Labusch model more appropriate for concentrated alloying and weak interaction [34], in both cases the mismatches of lattice parameter and elastic modulus between the solute and solvent atoms account for the additional resistance to gliding dislocations. Likewise, given that TB migration was accommodated with disconnections (as indicated in Figures 2 and 3), their mobility may also depend on the concentration and species of the solutes present on TBs, even if segregation was absent there. In particular, first-principles calculations [17] suggested that Mo and W solutes in Ni have almost identical lattice mismatch, but W leads to notably greater elastic mismatch than Mo does. The relative change of lattice size was calculated to be 0.19% between $Ni_{71}Mo$ and Ni and 0.20% between $Ni_{71}W$ and Ni, while the relative change of bulk modulus was 0.31% and 0.66%, respectively [17]. These account for a $6 \sim 10\%$ higher strength contributed by the same amount of W than Mo solutes as interacting with edge dislocations. Therefore, a greater resistance to detwinning is also expected for the W-rich specimens than the Mo-rich specimens, which aligns, at least qualitatively, with their difference in thermal stability that was uncovered in the current study.

Regarding the formation of carbides at the extremes of *in situ* heating, we note that C was involved in the attachment of the thin foils onto the heating chips and can readily diffuse on the surfaces and along the columnar GBs at elevated temperatures, although the as-made specimens at RT showed no segregation of C to the GBs. It is also probable that formation of carbides consumed Mo and W solutes and led to remarkable coarsening of the nanotwinned grains above 600°C or 800°C. Carbide precipitates were also observed in the as-deposited films ($\sim 30\,\mu m$ thick) after annealing in a vacuum furnace [15], but incorporation of C from the untreated surfaces may be expected there as well. Using the bulk diffusion coefficient of C in Ni [35], the diffusion depth is estimated to be $\sim 2.5\,\mu m$ at 600°C (5 min) and $\sim 77\,\mu m$ at 800°C (1 h), and diffusion along GBs is expected to be even faster. Therefore, the diffusion of C is sufficient to penetrate the whole specimen in either condition, which also calls for regulation of C uptake if nanotwinned Ni alloys are to be utilized in high temperature environments.

Conclusion

In summary, Mo-rich and W-rich nanotwinned Ni-Mo-W alloys were observed to undergo microstructural evolution in two stages during *in situ* heating, i.e. migration of twin boundaries and grain boundaries at intermediate temperatures and rapid formation of carbide precipitates at high temperatures. Our comparative studies show that W is more effective in stabilizing the microstructure than Mo is. While the influence of alloy composition on thermal stability cannot be attributed to variations in melting temperature, stacking fault energy, or solute diffusivities, consideration of classic solid solution strengthening mechanisms points to the importance of elastic modulus mismatch between solute and solvent atoms in inhibiting detwinning and stabilizing nanotwins.

Acknowledgements

We are grateful to Dr. Gianna Valentino and Prof. Jessica Krogstad for help in thin film deposition. We thank Dr. Jim Ciston for assistance in electron microscope operation at the Molecular Foundry (NCEM). Electron microscopy facilities were also provided by the Materials Characterization and Processing Center at Johns Hopkins University.

Disclosure statement

No potential conflict of interest was reported by the authors.

Funding

This work was supported by the U.S. Department of Energy, Basic Energy Sciences, under grant number DE-FG02-07ER4 6437. Work at the Molecular Foundry (NCEM) was supported by the U.S. Department of Energy, Basic Energy Sciences, under contract number DE-AC02-05CH11231.

ORCID

Ruopeng Zhang http://orcid.org/0000-0001-7677-4051

References

[1] Lu K, Lu L, Suresh S. Strengthening materials by engineering coherent internal boundaries at the nanoscale. Science. 2009;324:349–352. doi: 10.1126/science.1159610

[2] Huang Q, Yu D, Xu B, et al. Nanotwinned diamond with unprecedented hardness and stability. Nature. 2014;510:250–253. doi: 10.1038/nature13381

[3] Zhao S, Zhang R, Yu Q, et al. Cryoforged nanotwinned titanium with ultrahigh strength and ductility. Science. 2021;373:1363–1368. doi: 10.1126/science.abe7252
[4] Lu L, Shen Y, Chen X, et al. Ultrahigh strength and high electrical conductivity in copper. Science. 2004;304:422–426. doi: 10.1126/science.1092905
[5] Lu L, Chen X, Huang X, et al. Revealing the maximum strength in nanotwinned copper. Science. 2009;323:607–610. doi: 10.1126/science.1167641
[6] Pan Q, Zhou H, Lu Q, et al. History-independent cyclic response of nanotwinned metals. Nature. 2017;551:214–217. doi: 10.1038/nature24266
[7] Anderoglu O, Misra A, Wang H, et al. Thermal stability of sputtered Cu films with nanoscale growth twins. J Appl Phys. 2008;103:094322. doi: 10.1063/1.2913322
[8] Brons JG, Padilla II HA, Thompson GB, et al. Cryogenic indentation-induced grain growth in nanotwinned copper. Scr Mater. 2013;68:781–784. doi: 10.1016/j.scriptamat.2012.12.026
[9] Bufford D, Wang H, Zhang X. Thermal stability of twins and strengthening mechanisms in differently oriented epitaxial nanotwinned Ag films. J Mater Res. 2013;28:1729–1739. doi: 10.1557/jmr.2013.50
[10] Krogstad JA, Keimel C, Hemker KJ. Emerging materials for microelectromechanical systems at elevated temperatures. J Mater Res. 2014;29:1597–1608. doi: 10.1557/jmr.2014.183
[11] Velasco L, Hodge AM. The mobility of growth twins synthesized by sputtering: tailoring the twin thickness. Acta Mater. 2016;109:142–150. doi: 10.1016/j.actamat.2016.02.042
[12] Kurz SJB, Ensslen C, Welzel U, et al. The thermal stability of Ni-Mo and Ni-W thin films: solute segregation and planar faults. Scr Mater. 2013;69:65–68. doi: 10.1016/j.scriptamat.2013.03.006
[13] Li Q, Cho J, Xue S, et al. High temperature thermal and mechanical stability of high-strength nanotwinned Al alloys. Acta Mater. 2019;165:142–152. doi: 10.1016/j.actamat.2018.11.011
[14] Sim GD, Krogstad JA, Reddy KM, et al. Nanotwinned metal MEMS films with unprecedented strength and stability. Sci Adv. 2017;3:e1700685. doi: 10.1126/sciadv.1700685
[15] Sim GD, Krogstad JA, Xie KY, et al. Tailoring the mechanical properties of sputter deposited nanotwinned nickel-molybdenum-tungsten films. Acta Mater. 2018;144:216–225. doi: 10.1016/j.actamat.2017.10.065
[16] Valentino GM, Krogstad JA, Weihs TP, et al. Tailoring the coefficient of thermal expansion of ternary nickel alloys through compositional control and non-contact measurements. J Alloys Compd. 2020;833:155024. doi: 10.1016/j.jallcom.2020.155024
[17] Shang SL, Zacherl CL, Fang HZ, et al. Effects of alloying element and temperature on the stacking fault energies of dilute Ni-base superalloys. J Phys Condens Matter. 2012;24:505403. doi: 10.1088/0953-8984/24/50/505403
[18] Pavlovic A, Suresh Babu V, Seehra MS. High-temperature thermal expansion of binary alloys of Ni with Cr, Mo and Re: a comparison with molecular dynamics simulations. J Phys Condens Matter. 1996;8:3139–3149. doi: 10.1088/0953-8984/8/18/007
[19] Dosovitskiy G, Samoilenkov S, Kaul A, et al. Thermal expansion of Ni-W, Ni-Cr, and Ni-Cr-W alloys between room temperature and 800°C. Int J Thermophys. 2009;30:1931–1937. doi: 10.1007/s10765-009-0660-9
[20] Jin K, Mu S, An K, et al. Thermophysical properties of Ni-containing single-phase concentrated solid solution alloys. Mater Des. 2017;117:185–192. doi: 10.1016/j.matdes.2016.12.079
[21] https://www.protochips.com/products/fusion/fusion-select-components/
[22] Xu L, Xu D, Tu KN, et al. Structure and migration of (112) step on (111) twin boundaries in nanocrystalline copper. J Appl Phys. 2008;104:113717. doi: 10.1063/1.3035944
[23] Wang J, Li N, Anderoglu O, et al. Detwinning mechanisms for growth twins in face-centered cubic metals. Acta Mater. 2010;58:2262–2270. doi: 10.1016/j.actamat.2009.12.013
[24] Wang YM, Sansoz F, LaGrange T, et al. Defective twin boundaries in nanotwinned metals. Nat Mater. 2013;12:697–702. doi: 10.1038/nmat3646
[25] Detor AJ, Schuh CA. Tailoring and patterning the grain size of nanocrystalline alloys. Acta Mater. 2007;55:371–379. doi: 10.1016/j.actamat.2006.08.032
[26] Trelewicz JR, Schuh CA. Grain boundary segregation and thermodynamically stable binary nanocrystalline alloys. Phys Rev B. 2009;79:094112. doi: 10.1103/PhysRevB.79.094112
[27] Turchi PEA, Kaufman L, Liu ZK. Modeling of Ni–Cr–Mo based alloys: part I—phase stability. Calphad. 2006;30:70–87. doi: 10.1016/j.calphad.2005.10.003
[28] Takeuchi A, Inoue A. Classification of bulk metallic glasses by atomic size difference, heat of mixing and period of constituent elements and its application to characterization of the main alloying element. Mater Trans. 2005;46:2817–2829. doi: 10.2320/matertrans.46.2817
[29] Cahn JW. The impurity-drag effect in grain boundary motion. Acta Metall. 1962;10:789–798. doi: 10.1016/0001-6160(62)90092-5
[30] Campbell CE, Boettinger WJ, Kattner UR. Development of a diffusion mobility database for Ni-base superalloys. Acta Mater. 2002;50:775–792. doi: 10.1016/S1359-6454(01)00383-4
[31] Liu XJ, Hu HH, Han JJ, et al. Assessment of the diffusional mobilities in fcc Ni-Nb and fcc Ni-Mo alloys. Calphad. 2012;38:140–145. doi: 10.1016/j.calphad.2012.05.003
[32] Chen J, Zhao J, Zhang L, et al. Atomic mobilities in fcc Ni-rich Ni-X (X = Rh, Ta, W. Re, and Ir) systems. Calphad. 2019;65:316–325. doi: 10.1016/j.calphad.2019.03.013
[33] Fleischer RL. Substitutional solution hardening. Acta Metall. 1963;11:203–209. doi: 10.1016/0001-6160(63)90213-X
[34] Labusch R. A statistical theory of solid solution hardening. Phys Stat Solidi (b). 1970;41:659–669. doi: 10.1002/pssb.19700410221
[35] Lander JJ, Kern HE, Beach AL. Solubility and diffusion coefficient of carbon in nickel: reaction rates of nickel-carbon alloys with barium oxide. J Appl Phys. 1952;23:1305–1309. doi: 10.1063/1.1702064

Appendix A. characterization of solute distribution at TBs

Additional thin foils of the two alloys (Mo-rich and W-rich) in this study were extracted from the same pieces of as-deposited films that were used to fabricate the *in situ* heated specimens. These foils were also extracted using 30 kV Ga^+ FIB and polished to 100 nm or less in thickness using 2 kV Ga^+. Atom-resolved STEM and XEDS were performed using a probe-corrected JEOL Grand ARM II microscope operated at 300 kV.

Figure A1 shows representative characterization results of the two alloys. Densely packed nanotwins are exhibited in HAADF images (a1) and (b1), and line-scan profiles were measured normal to the arrays of (111) TBs using a line width of 6 nm and a step size of 0.1 nm; the concentrations of Mo and W as well as the intensity of HAADF image signal are then displayed in (a2) and (b2). It is first noted that the HAADF intensity profiles in both alloys showed discernible long-range variation normal to the TBs, with the peak positions appearing to coincide with several TBs, which are marked with '+' in (a2) and (b2). The magnitude of such variation was even greater in the W-rich foil (b1) than in the Mo-rich foil (a1), although both images were recorded and processed under identical conditions. Since the HAADF intensity strongly scales with the (average) atomic number, which is known as the 'Z-contrast', it is speculated that the marked TBs were also associated with the segregation of Mo or W solutes.

On the other hand, the compositional profiles in (a2) and (b2) apparently show no difference with statistical significance at the marked TBs. Averaging over a window of 0.5 nm (which accounts for the beam broadening through foil thickness) across these TBs, the excess concentrations were calculated as:

$$\Delta_{Mo} = 0.11 \pm 0.15, \Delta_W = 0.14 \pm 0.08,$$
$$\text{in the Mo - rich foil (a2);}$$
$$\Delta_{Mo} = 0.07 \pm 0.09, \Delta_W = 0.13 \pm 0.12,$$
$$\text{in the W - rich foil (b2).}$$

These results suggest that either species was not effectively segregating to the TBs, and no difference in the composition at TBs was discernable between the Mo-rich and W-rich foils, so then their distinct profiles of HAADF intensity remain unexplained.

Taken as a whole, although both STEM images and XEDS measurements provided faint hints of solute segregation at TBs, these results fell short of interconsistency and statistical significance. Convincing evidence of the nature of solute segregation and in particular the difference between Mo-rich and W-rich specimens is still lacking. Nevertheless, one should notice that the inhomogeneity of solute distribution in the TB planes may be finite in both magnitude and length scale and prone to be erased by averaging through thickness; three-dimensional characterization (e.g. atom-probe tomography) may provide a clearer delineation of such nanostructured alloys but is beyond the scope of current study.

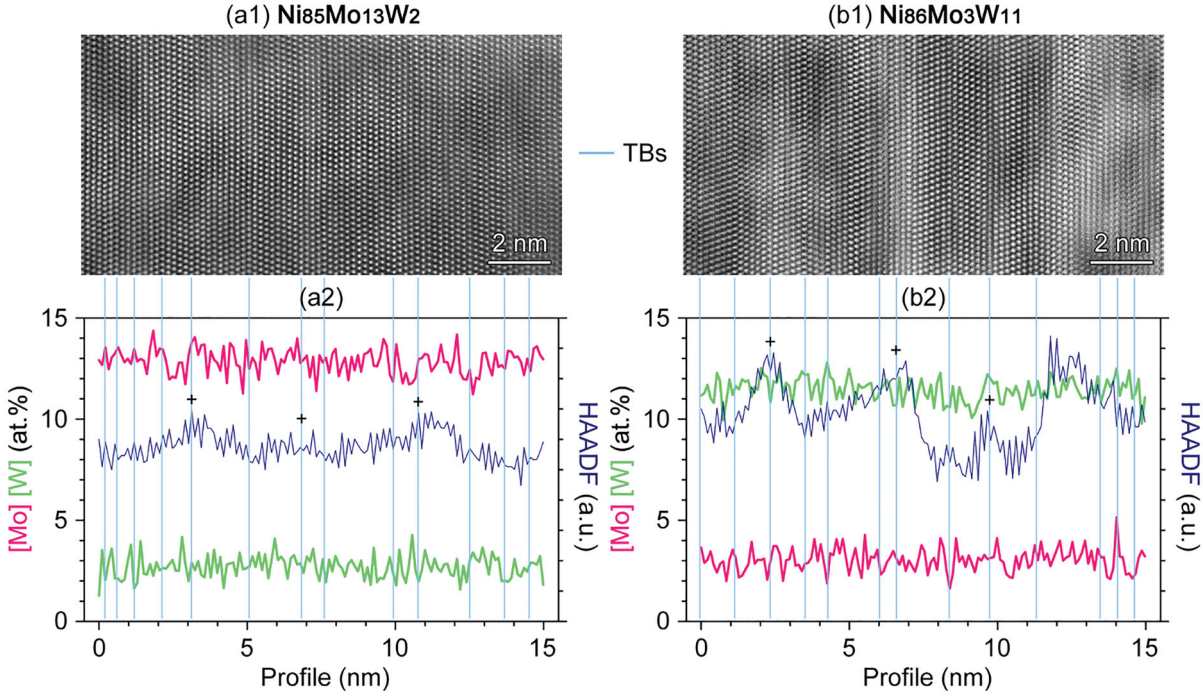

Figure A1. STEM-XEDS characterization of as-deposited nanotwinned alloys: **(a)** Mo-rich film; **(b)** W-rich film. (a1) and (b1) show HAADF images, (111) TBs are marked with light blue lines. (a2) and (b2) show line-scan profiles of the atomic concentrations of Mo (pink) and W (green) as well as the intensity of HAADF signal (dark blue) measured normal to the TBs. Peaks in the long-range variations of HAADF intensity are marked with '+'. Note that the high-frequency variations correspond to the periodicity of (111) atomic planes.